

## 4B.4 A LARGE EDDY SIMULATION MODEL OF HIGH WIND MARINE BOUNDARY LAYERS ABOVE A SPECTRUM OF RESOLVED MOVING WAVES

Peter P. Sullivan<sup>1\*</sup>, James C. McWilliams<sup>2</sup> and Tihomir Hristov<sup>3</sup>

<sup>1</sup>National Center for Atmospheric Research, Boulder, CO

<sup>2</sup>Department of Atmospheric and Oceanic Sciences, UCLA, Los Angeles, CA

<sup>3</sup>Department of Mechanical Engineering, The Johns Hopkins University, Baltimore, MD

### 1. INTRODUCTION

An improved understanding of the interaction of winds, waves, and currents in the upper ocean at scales of individual waves and wave groups is needed to further develop the next generation of climate, weather, and wave forecast models. For example, coupled wind-wave-ocean models (Chen et al., 2007; Black et al., 2007) are viewed as critical tools for accurate prediction of tropical cyclone intensity and track forecasts, but these modeling systems employ a suite of parameterizations that are largely statistical descriptions of the wind-wave interactions that generate the critical momentum and scalar fluxes. These forecast models do not account for the important phase relationships between winds, waves and currents, *e.g.*, the spatial and temporal intermittency of wave breaking that occurs in moderate to high winds (see figure 1). Also, there is a growing appreciation that wave-current interactions are important for the upper ocean boundary layer (Sullivan and McWilliams, 2010), and thus for climate predictions, and that remotely generated swell and non-equilibrium wave states can play an important and critical role in the surface-layer dynamics of the atmospheric planetary boundary layer (PBL) (Hanley et al., 2010; Sullivan and McWilliams, 2010).

The present work describes our recent developments in coupling a turbulence-resolving large-eddy simulation (LES) of the atmospheric PBL to a three-dimensional time-dependent resolved surface wavefield. This builds on our past efforts which coupled a turbulent boundary-layer flow with a single monochromatic wave (Sullivan et al., 2000; Sullivan and McWilliams, 2002; Sullivan et al., 2008). The computational method described here allows for nearly arbitrary 3D wavefields, *i.e.*, the sea surface elevation  $h = h(x, y, t)$ , as a surface boundary condition. The spatial scales of the resolved turbulence and waves are  $O(m)$  up to the scale of the PBL height. At present, the waves are externally imposed based on empirical wave spectra. Ultimately the wavefields will

be direct observations of the sea surface from field campaigns. High resolution simulations of PBL turbulence in the presence of surface waves has the potential to provide new insight into the dynamics of air-sea coupling at small scales. The jump in massively parallel computational resources facilitates the coupling of winds and waves in turbulence resolving simulations.

### 2. LES ALGORITHM WITH MOVING WAVES

An LES model for an atmospheric PBL with a stationary undulating lower boundary is described in Sullivan et al. (2010). They outline the algorithm, numerical details, code parallelization, and present results for boundary-layer flows over and around two- and three-dimensional orography. Here we build on those developments but focus on the additional complications caused by the temporal movement of the 3D lower surface. In the description of the model equations, given in Section 2.2, the following notation is used:  $\overline{\rho \mathbf{u}}$  denotes the Cartesian components of momentum,  $\overline{\theta}$  is virtual potential temperature,  $e$  is the subgrid-scale energy, and  $\overline{\Pi}$  is the pressure variable. Quantities with an overbar ( $\overline{\quad}$ ) are interpreted as LES spatially filtered variables.

#### 2.1 Coordinate transformation

We follow Sullivan et al. (2010) and adapt our LES model with a flat bottom to the situation with a three-dimensional time-dependent boundary shape  $h = h(x, y, t)$  by applying a transformation to the physical space coordinates  $(x, y, z)$  that maps them onto computational coordinates  $(\xi, \eta, \zeta)$ . The computational mesh in physical space is surface following, non-orthogonal, and time varying. Also, vertical gridlines are held fixed at a particular  $(x, y)$  location on the surface but the lines are permitted to undergo vertical translation as a function of time  $t$ , *i.e.*, vertical gridlines are wave following. The transformation which obeys these constraints and maps the physical domain to a flat computational domain  $\mathbf{x} \Rightarrow \xi$  is the rule:

\*corresponding author address: Peter P. Sullivan, National Center for Atmospheric Research, P. O. Box 3000, Boulder, CO 80307-3000; email: pps@ucar.edu

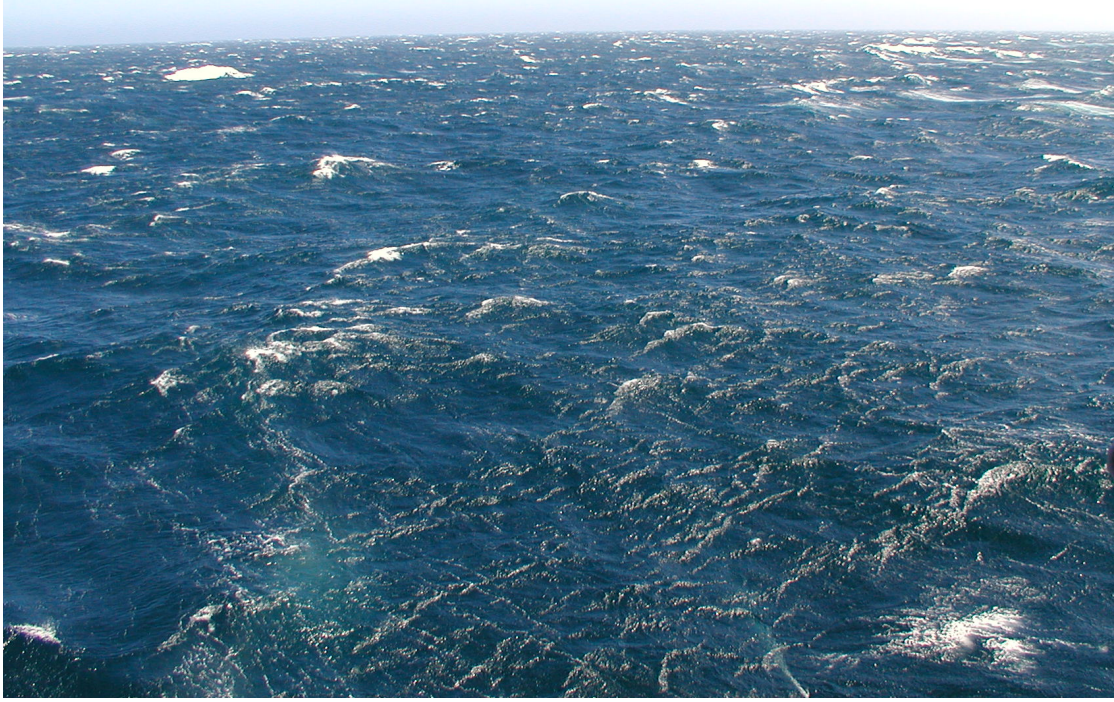


Figure 1: Photograph of the sea surface generated by winds of approximately  $15 \text{ m s}^{-1}$  during the High Resolution Air-Sea Interaction (Hi-Res) field campaign carried out in June 2010. Notice the extensive white capping generated by large-scale plunging and spilling breakers and, in the foreground, a web of small-scale breakers. The photograph is taken from the R/V Floating Instrument Platform (FLIP) courtesy of Tihomir Hristov. For a description of Hi-Res see <http://airsea.ucsd.edu/hires/>.

$$\tau = t \quad (1a)$$

$$\xi = \xi(x) = x \quad (1b)$$

$$\eta = \eta(y) = y \quad (1c)$$

$$\zeta = \zeta(t, x, y, z). \quad (1d)$$

The differential metrics  $\partial x_i / \partial \xi_j$  and  $\partial \xi_i / \partial x_j$ , which are needed in formulating the LES model, are connected through the mapping transformation. Thus given the rules in (1) we have the reduced set of non-zero metric relationships:

$$\zeta_t = -z_t J \quad (2a)$$

$$\zeta_x = -z_\xi J \quad (2b)$$

$$\zeta_y = -z_\eta J \quad (2c)$$

$$\zeta_z = 1/z_\zeta = J \quad (2d)$$

$$\xi_x = \eta_y = 1 \quad (2e)$$

where  $J$  is the Jacobian. The time dependence of the mapping appears in (2a) where  $z_t = \partial z / \partial t$  is the *grid speed*, i.e., the vertical velocity of individual gridpoints.

## 2.2 LES equations in curvilinear coordinates with time dependence

The LES equations in curvilinear coordinates are derived in a straightforward manner by applying the chain rule for differentiation but we pay close attention to the transformation of the material derivative  $D(\cdot)/Dt$  and the mass conservation equation. The set of LES equations in computational coordinates under the transformation (1) and (2) are:

$$\frac{\partial U_i}{\partial \xi_i} = 0 \quad (3a)$$

$$\frac{\partial}{\partial t} \left( \frac{1}{J} \right) = \frac{\partial z_t}{\partial \zeta} \quad (3b)$$

$$\frac{\partial}{\partial t} \left( \frac{\bar{u}_i}{J} \right) + \frac{\partial}{\partial \xi_j} [(U_j - \delta_{3j} z_t) \bar{u}_i] = \mathcal{F}_i \quad (3c)$$

$$\frac{\partial}{\partial t} \left( \frac{\bar{\theta}}{J} \right) + \frac{\partial}{\partial \xi_j} [(U_j - \delta_{3j} z_t) \bar{\theta}] = \mathcal{M} \quad (3d)$$

$$\frac{\partial}{\partial t} \left( \frac{e}{J} \right) + \frac{\partial}{\partial \xi_j} [(U_j - \delta_{3j} z_t) e] = \mathcal{R} \quad (3e)$$

$$\frac{\partial}{\partial \xi_i} \left[ \frac{1}{J} \frac{\partial \xi_i}{\partial x_j} \frac{\partial \xi_m}{\partial x_j} \frac{\partial \Pi}{\partial \xi_m} \right] = \mathcal{S} \quad (3f)$$

The equations are expressed in strong conservation form using the ‘‘contravariant flux’’ velocity

$$U_i = \frac{\bar{u}_j}{J} \frac{\partial \xi_j}{\partial x_i}. \quad (4)$$

(3a) is the mass conservation (continuity) equation, (3c) is the momentum transport equation, (3d) is the scalar transport equation, (3e) is the subgrid-scale energy transport equation, and (3f) is the pressure Poisson equation. The right hand sides of (3) model physical processes in the marine atmospheric PBL, *e.g.*, pressure gradients, Coriolis rotation, divergence of subgrid-scale fluxes, buoyancy, and in the case of the SGS  $\epsilon$  equation also diffusion and dissipation.

The time dependence of the grid modifies the LES equations: the Jacobian appears inside the time tendency of each transport equation and as expected advection contains a contribution from the grid movement, *i.e.*, the total vertical flux of variable  $\psi$  depends on the difference between the physical velocity and grid speed  $(W - z_t)\psi$ . Also, as a consequence of writing the equations in strong conservation form we need to satisfy (3b) which is a simplified form of the so-called geometric or space conservation law (GCL) first discussed by Thomas and Lombard (1979). In our derivation, (3b) follows directly from considering the unsteady form of the mass conservation equation written in differential form. Thomas and Lombard (1979) and also Demirdžić and Perić (1990) derive the GCL by considering an integral form of the equations of motion. Inspection of (3) shows that if the velocity and scalar fields are set to constant values then the left hand sides of (3c-e) reduce to (3b). Hence our numerical method needs to satisfy our reduced form of the GCL discretely in order to prevent artificial sources and sinks from developing in the computational domain. Thus, the mixed pseudospectral finite-differencing spatial differencing evaluates the advective terms in (3c-e) in flux form and not the rotational form used by Moeng (1984) or skew-symmetric form used by Sullivan et al. (2000).

We use (3b) with our Runge-Kutta time stepping scheme in the following way: Given the wave height distribution at any future timestep, say  $t^{n+1}$ , we first pick the vertical distribution of gridpoints  $z(\xi, \eta, \zeta, t^{n+1})$  based on the computational domain height and  $h(\xi, \eta, t^{n+1})$ . We then insert the Runge-Kutta time stepping discretization in (3b) and solve for the required matching grid speed  $z_t$ . Since our time stepping is explicit the value of  $z_t$  diagnosed applies at the time level  $t^n$ . In other words, if the wavefield is imposed knowledge of its future shape is needed to diagnose the grid speed at an earlier time. This is analogous to our grid nesting scheme where the vertical velocity at a future time is imposed on a nested boundary (Sullivan et al., 1996).

We emphasize that the upper boundary of our computational domain is far from the lower surface and asymptotes to a flat level surface. As a result  $z_t$  varies with distance from the wave surface. This is different than the scheme proposed by Chalikov (1998) where the grid speed is equal to the vertical motion of the wavefield for all  $z$ . This implies that the computational mesh at any  $\zeta$ , including the upper boundary, mimics the shape of the lower surface. At the lower boundary  $z = h$ , the time rate of change of the wavy surface is

$$z_t \equiv h_t = w_o - h_\xi u_o - h_\eta v_o \quad (5)$$

where  $(u_o, v_o, w_o)$  are the orbital motions of the wavefield. The kinematical boundary condition is then  $W - z_t = 0$  so that there is no flow through the boundary. Notice the definition of  $W(z = h)$  given by (4) is consistent with (5). The surface grid movement also leads to subtleties in formulating the pressure Poisson equation and its boundary conditions.

### 2.3 Wavefield prescription

To complete our marine PBL LES we need to prescribe the surface wavefield. For the present computations we use empirical two-dimensional statistical wave spectra (*e.g.*, see Komen et al., 1994, p. 187)

$$E(k, \phi) = S(k) D(k, \phi) \quad (6)$$

where the amplitude  $S(k)$  and directional  $D(k, \phi)$  spectra depend on the wavenumber  $k = |\mathbf{k}| = |k_x \hat{\mathbf{i}} + k_y \hat{\mathbf{j}}|$ , wave direction  $\phi$  and surface wind speed  $U_{10}$ . For the amplitude spectrum we choose the classic Pierson-Moskowitz shape (Pierson and Moskowitz, 1964; Alves et al., 2003) while a simple directional spectrum is designed to emphasize long-crested waves with their spanwise axis oriented perpendicular to the wind direction  $D(k, \phi) = (\mathbf{k} \cdot \mathbf{U})^n$ . In physical space, the synthetic wavefield  $h(x, y, t)$  is constructed from a sum of plane waves

$$h(\mathbf{x}, t) = \sum_{\mathbf{k}} \hat{h}(\mathbf{k}) \exp[i(\mathbf{k} \cdot \mathbf{x} - \omega t)] \quad (7)$$

with the wave amplitudes  $\hat{h}(\mathbf{k})$  picked to match  $E(k, \phi)$ . The phases are chosen from a Gaussian distribution. Inside the LES, the wavefield is advanced in time using the linear dispersion relation  $\omega^2 = gk$  once the initial distribution of amplitudes is specified. (7) is efficiently evaluated using 2D Fast Fourier Transforms. Figure 2 shows a typical instantaneous 3D wavefield that is input at the bottom of the LES. Future computations will use the detailed phase-resolved wave measurements collected in the Hi-Res field campaign.

### 3. SIMULATIONS

A series of simulations with varying geostrophic wind  $U_g = (5, 7.5, 10, 15, 20)$  m s<sup>-1</sup> are carried out for a neutrally-stratified marine PBL in a domain  $(X_L, Y_L, Z_L) = (1200, 1200, 800)$  m using  $(N_x, N_y, N_z) = (512, 512, 128)$  gridpoints; thus the horizontal grid spacing  $\Delta x = \Delta y = 2.34$  m and the first vertical level is 1 m above the water. A slice of the computational mesh is given in figure 3. The initial temperature sounding  $\bar{\theta} = 300$  K up to the inversion height  $z_i = 400$  m, beyond this height  $\bar{\theta}$  increases linearly at  $3 \times 10^{-3}$  K m<sup>-1</sup>. The surface heating  $Q_* = 0$ , the surface roughness  $z_o = 0.0002$  m, and the Coriolis parameter  $f = 10^{-4}$  s<sup>-1</sup>. The wavefield is built, as discussed in Section 2.3, based on a wind speed of 15 m s<sup>-1</sup> and the phase speed of the peak in the spectrum  $C_p \sim 18$  m s<sup>-1</sup>. Thus the suite of simulations allows us to examine a wide variation of wave age from swell dominated to near wind-wave equilibrium. Table 1 lists bulk properties of the simulations, *viz.*, the geostrophic wind, wave age, and friction velocity  $u_*$ .  $U_{10}$  is the reference wind speed at a height of 10 m. The simulations are run for more than 50,000 timesteps using restart volumes with fully developed turbulence. The iteration count in the pressure Poisson solver is typically set to 30 and the calculations run on either 512 or 1024 computational cores.

Table 1: Simulation properties

Run	$U_g$ (m s <sup>-1</sup> )	$C_p/U_{10}$	$u_*$ (m s <sup>-1</sup> )
A	5	4.8	0.124
B	7.5	3.4	0.187
C	10	2.8	0.228
D	15	1.9	0.338
E	20	1.5	0.452

### 4. RESULTS

Previous field observations (Grachev and Fairall, 2001; Smedman et al., 1999), turbulence closure modeling (Hanley and Belcher, 2008; Makin, 2008), and our own idealized LES (Sullivan et al., 2008) all show that fast moving swell can induce marked changes in the atmospheric surface layer winds, *viz.*, an upward momentum flux from the ocean to the atmosphere, a low-level wind maximum, and departures from law-of-the-wall scaling. The preliminary LES computations performed here over a more realistic sea surface are in good qualitative agreement with the previous studies but suggest the impact of swell on the surface layer winds is sensitive to the content of the wave spectrum.

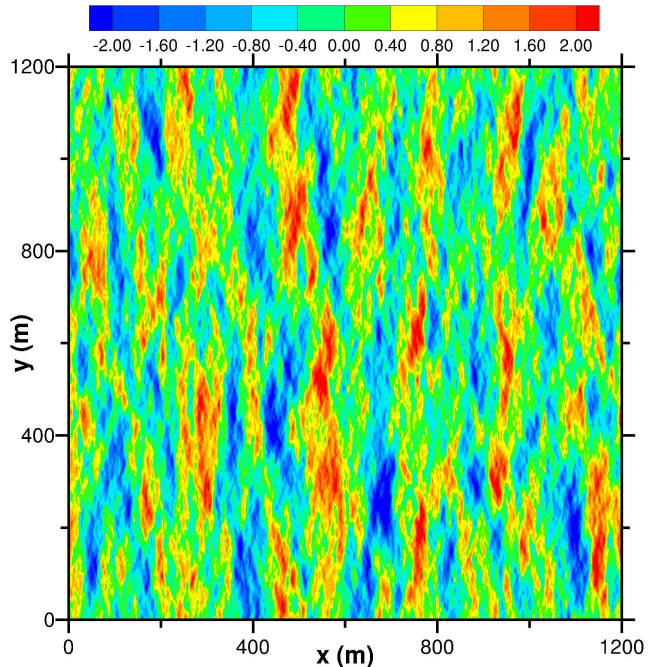


Figure 2: A snapshot of the wavefield height  $h(x, y, t)$  that is imposed at the bottom of the LES code.  $h$  is built from a sum of linear plane waves (7). Waves propagate left to right according to the dispersion relationship. The horizontal grid spacing matches the LES, *i.e.*,  $\Delta x = \Delta y = 2.5$  m. The color bar is in units of meters.

One of the surprising results from the present simulations is the significant impact of swell on the coherence and magnitude of the near-surface pressure fluctuations. This is illustrated in figure 4 where we compare  $p'/\rho$  for two levels of wind forcing  $U_g = (5, 20)$  m s<sup>-1</sup>, *i.e.*, a low-wind situation with swell and a high wind case approaching wind-wave equilibrium. The difference in the pressure signals is striking and even more remarkable in animations of the pressure field. In the low-wind swell case there is a very strong correlation between  $p'/\rho < 0$  and wave crests and similarly between  $p'/\rho > 0$  and wave troughs that extends over the depth of the surface layer. Inspection of the flow visualization and animations reveals that the strong correlation persists across the range of resolved waves, *i.e.*, both large and small scale waves appear to induce a similar pressure pattern. The coherence of the wave induced pressure field can extend to 20 m or more depending on the amplitude of the underlying wave. Also, the pressure signatures propagate at the speed of the wavefield, additional evidence that the signals are generated by surface waves and not atmospheric processes. These are clear signatures of “wave pumping” by the surface wavefield on the atmosphere. The ampli-

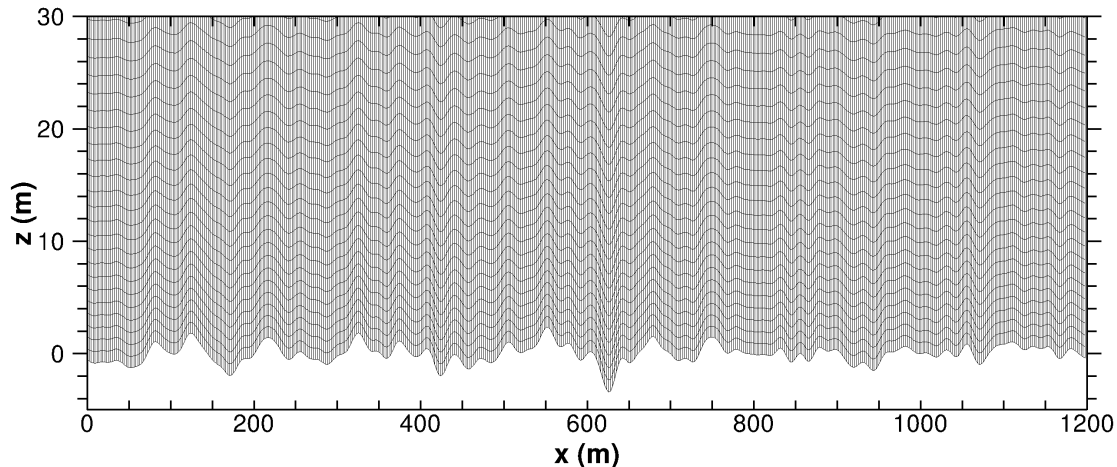


Figure 3: An instantaneous  $x - z$  slice of the 3D time varying computational mesh in the lowest portion of the PBL. The  $(\xi, \eta)$  gridlines become level surfaces at about 100 m above the water. Only a fraction of the grid is displayed.

tude of the wave spectrum (and hence the level of wave forcing) is held constant in our simulations but the magnitude of the turbulence, as measured by  $u_*$ , increases substantially with increasing wind speed. The structure of the near surface pressure field is a result of these two competing effects. At low winds coherent pressure signals are generated by the wave motions when the turbulence is weak but this coherence is destroyed by strong turbulence at higher winds.

Figure 5 shows that the impact of wave age also appears in the vertical velocity fields. In the low-wind swell regime we observe large-amplitude large-scale fluctuations in  $w'$ . At higher winds the spatial coherence of  $w'$  is destroyed by strong turbulence. Note each panel in figure 5 is sampled at the sample height above the wavefield. Also, the fields are made dimensionless by friction velocity  $u_*$  which further illustrates the strong impact of the wave motions on the winds in the surface layer.

In figure 6 we compare vertical profiles of the mean wind speed and turbulence variances for the different simulations. These statistics are computed by averaging in computational coordinates, *i.e.*, across horizontal planes at constant vertical height  $\zeta$ . Similar to Sullivan et al. (2008) we find that the wind speed and turbulence variances depend on wave age. At high winds as the simulations approach wind-wave equilibrium, the non-dimensional wind profile  $\langle U \rangle / u_*$  smoothly approaches the variation predicted by law-of-the-wall. Significant differences are observed for the cases dominated by swell: the surface layer winds are accelerated compared to rough wall scaling. As suggested by the flow visualization, the turbulence variances respond to the wave motion in dramatic ways. The horizontal and vertical variances are significantly enhanced by the motion of the

wave surface in the low-wind cases. Even though the turbulence is relatively weak the turbulence variances are large near the wave surface due to wave pumping.

## 5. SUMMARY

A large-eddy simulation (LES) model for the marine atmospheric planetary boundary layer (PBL) is coupled to a 3D time-dependent surface gravity wavefield. A coordinate transform from physical to computational space is used that accounts for vertical movement of the mesh in physical space. We use the geometric conservation law (GCL) (Thomas and Lombard, 1979) to solve for the grid speeds that enter into the advection of momentum and scalars. The algorithm is used to carry out a series of simulations over a broadband moving wavefield that conforms to a Pierson-Moskowitz wave spectrum. The wave age  $C_p/U_{10} = [1.5, 4.8]$  varies from near wind-wave equilibrium to a low-wind swell dominated regime. In the low wind cases we find features similar to previous observational and modeling investigations: the surface layer winds show clear departures from rough wall law-of-the-wall scaling. The coherence and magnitude of the pressure field  $p'/\rho$  depends critically on the motion of the underlying wavefield and the turbulence level.

*Acknowledgments:* The authors and their research are supported by the Office of Naval Research, Physical Oceanography program. P. Sullivan is also supported by the National Science Foundation through the National Center for Atmospheric Research. Computational resources were supplied by NCAR and the Department of Defense High Performance Computing. NCAR is spon-

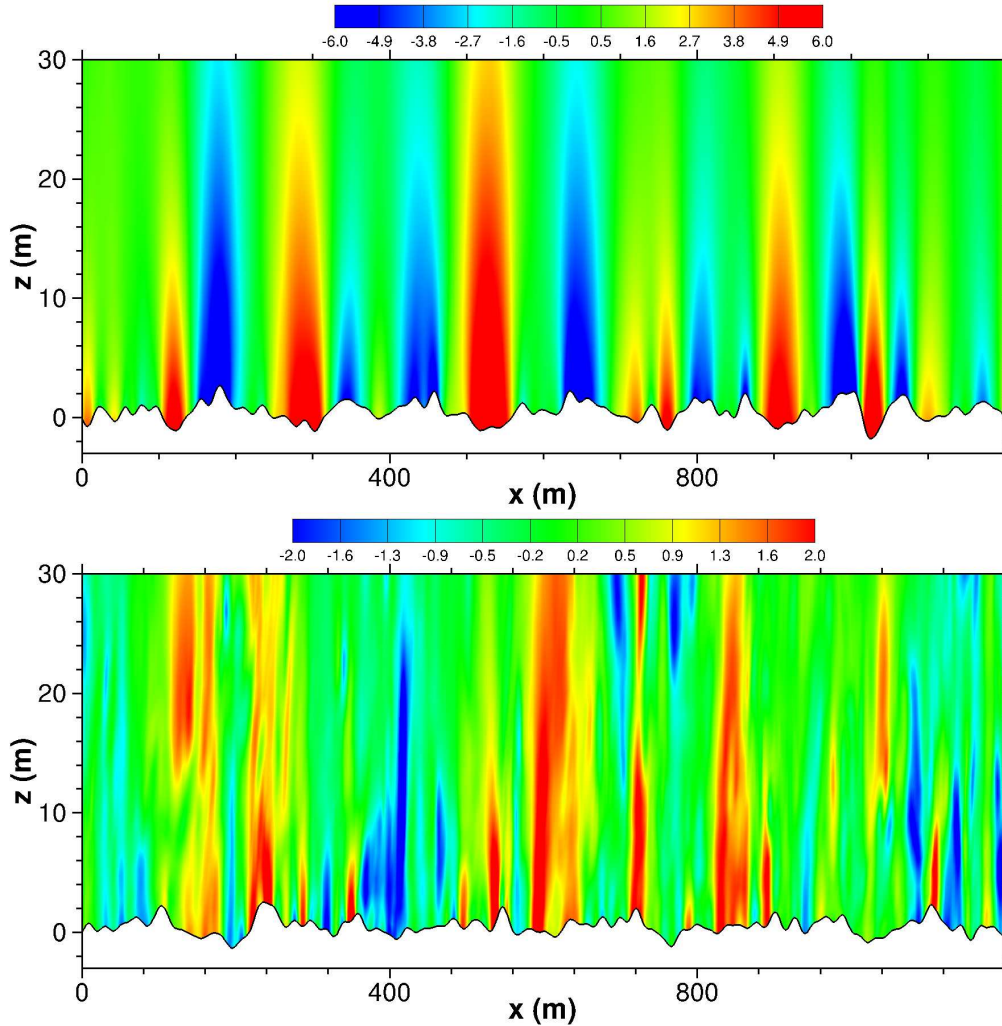


Figure 4: Snapshot of static pressure fluctuations  $p'/\rho$  in an  $x-z$  plane near the water surface. The upper panel is a swell dominated regime with wave age  $\sim 4.8$  while the lower panel is a case near wind-wave equilibrium with wave age  $\sim 1.4$ . The wave spectrum is a Pierson-Moskowitz spectrum. Notice the coherence between the wave field and the pressure fluctuations in the case with swell. The color bar is in units of  $\text{m s}^{-2}$  and the range is different between the two cases.

sored by the National Science Foundation. Any opinions, findings, and conclusions or recommendations expressed in this publication are those of the author(s) and do not necessarily reflect the views of the National Science Foundation.

## REFERENCES

- Alves, J. G. M., M. L. Banner, and I. R. Young, 2003: Revisiting the Pierson-Moskowitz asymptotic limits for fully developed wind waves, *J. Phys. Oceanogr.*, **33**, 1301–1323.
- Black, P., E. D’Asaro, W. Drennan, J. French, P. Niiler, T. Sanford, E. Terrill, E. Walsh, and J. Zhang, 2007: Air-sea exchange in hurricanes: Synthesis of observations from the Coupled Boundary Layers Air-Sea Transfer experiment, *Bull. Amer. Meteorol. Soc.*, **88**, 357–374.
- Chalikov, D., 1998: Interactive modeling of surface waves and boundary layer, in *Ocean Wave Measurement and Analysis: Proceedings of the Third International Symposium Waves 97*, edited by B. L. Edge, J. M. Hemsley, and Y. Goda, pp. 1525–1539, American Society of Civil Engineers.
- Chen, S. S., J. F. Price, W. Zhao, M. A. Donelan, and E. J. Walsh, 2007: The CBLAST-Hurricane program and the next-generation fully coupled atmosphere-wave-

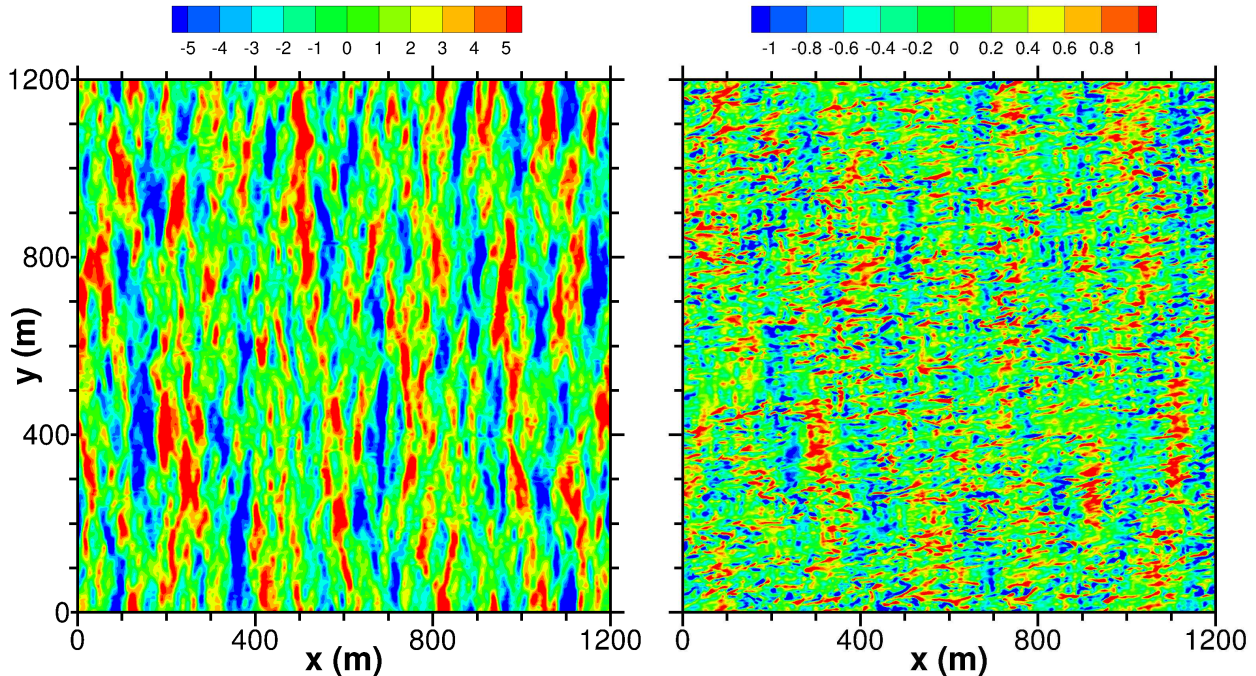


Figure 5: Snapshot of resolved vertical velocity fluctuations  $w'/u_*$  in a wave following  $x-y$  plane near the water surface  $\zeta = 2.5$  m. The left panel is a swell dominated regime with wave age  $\sim 4.8$  while the right panel is a case near wind-wave equilibrium with wave age  $\sim 1.4$ . The wave spectrum at the bottom of the PBLs is the same. Notice the range of the color bar is different between the two cases. The (normalized) fluctuations in the wind-wave equilibrium case are smaller.

- ocean models for hurricane research and prediction, *Bull. Amer. Meteorol. Soc.*, **88**, 311–317.
- Demirdžić, I. and M. Perić, 1990: Finite volume method for prediction of fluid flow in arbitrarily shaped domains with moving boundaries, *International Journal for Numerical Methods in Fluids*, **10**, 771–790.
- Grachev, A. A. and C. W. Fairall, 2001: Upward momentum transfer in the marine boundary layer, *J. Phys. Oceanogr.*, **31**, 1698–1711.
- Hanley, K. E. and S. E. Belcher, 2008: Wave-Driven wind jets in the marine atmospheric boundary layer, *J. Atmos. Sci.*, **65**, 2646–2660.
- Hanley, K. E., S. E. Belcher, and P. P. Sullivan, 2010: A global climatology of wind-wave interaction, *J. Phys. Oceanogr.*, **40**, 1263–1282.
- Komen, G. J., L. Cavaleri, M. Donelan, K. Hasselmann, S. Hasselmann, and P. A. E. M. Janssen, 1994: *Dynamics and Modelling of Ocean Waves*, Cambridge University Press, 532 pp.
- Makin, V. K., 2008: On the possible impact of a following-swell on the atmospheric boundary layer, *Boundary-Layer Meteorol.*, **129**, 469–478.
- Moeng, C.-H., 1984: A large-eddy simulation model for the study of planetary boundary-layer turbulence, *J. Atmos. Sci.*, **41**, 2052–2062.
- Pierson, W. J. and L. Moskowitz, 1964: A proposed spectral form for fully developed wind seas based on the similarity theory of S. A. Kitaigorodskii, *J. Geophys. Res.*, **69**, 5181–5190.
- Smedman, A., U. Höglström, H. Bergström, and A. Rutgersson, 1999: A case study of air-sea interaction during swell conditions, *J. Geophys. Res.*, **104**, 25833–25851.
- Sullivan, P. P., J. B. Edson, T. Hristov, and J. C. McWilliams, 2008: Large eddy simulations and observations of atmospheric marine boundary layers above non-equilibrium surface waves, *J. Atmos. Sci.*, **65**, 1225–1245.
- Sullivan, P. P. and J. C. McWilliams, 2002: Turbulent flow over water waves in the presence of stratification, *Phys. Fluids*, **14**, 1182–1195.

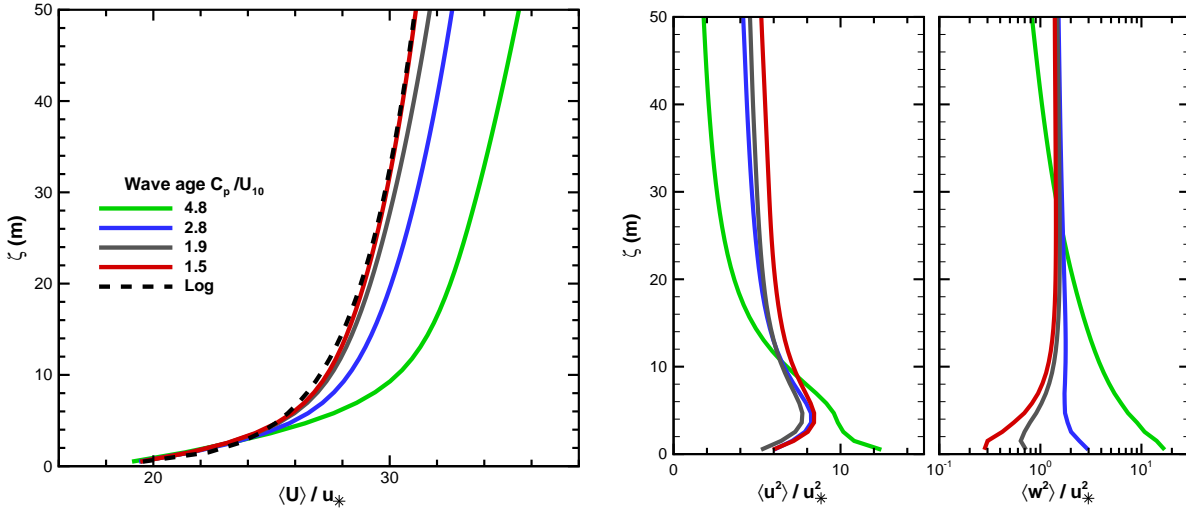


Figure 6: Vertical profiles of wind speed (left panel) and turbulence variances (right panels) for different values of wave age  $C_p/U_{10}$ . Friction velocity  $u_*$  is used for normalization. The dashed black line is the rough wall formula  $U/u_* = \ln(z/z_o)/\kappa$ , where  $\kappa = 0.4$ . Temporal and spatial averaging is used to make the statistics. The spatial averaging is over  $\xi - \eta$  planes, *i.e.*, at constant  $\zeta$ .

—, 2010: Dynamics of winds and currents coupled to surface waves, *Ann. Rev. Fluid Mech.*, **42**, 19–42.

Sullivan, P. P., J. C. McWilliams, and C.-H. Moeng, 1996: A grid nesting method for large-eddy simulation of planetary boundary layer flows, *Boundary-Layer Meteorol.*, **80**, 167–202.

—, 2000: Simulation of turbulent flow over idealized water waves, *J. Fluid Mech.*, **404**, 47–85.

Sullivan, P. P., E. G. Patton, and K. W. Ayotte, 2010: Turbulent flow over and around sinusoidal bumps, hills, gaps and craters derived from large eddy simulations, in *19th Amer. Meteorol. Soc. Symp. on Boundary Layer and Turbulence*, Keystone, CO.

Thomas, P. D. and C. K. Lombard, 1979: Geometric conservation law and its application to flow computations on moving grids, *AIAA Journal*, **17**, 1030–1037.